Journal of Materials Chemistry A

ROYAL SOCIETY OF CHEMISTRY

PAPER

View Article Online
View Journal | View Issue

Cite this: J. Mater. Chem. A, 2020, 8, 25148

Heteroporous bifluorenylidene-based covalent organic frameworks displaying exceptional dye adsorption behavior and high energy storage†

Ahmed F. M. EL-Mahdy, [ab] Mohamed Barakat Zakaria, [cde] Hao-Xin Wang,[a] Tao Chen, [f] Yusuke Yamauchi [ceg] and Shiao-Wei Kuo *[ah]

Received 26th July 2020
Accepted 3rd November 2020

DOI: 10.1039/d0ta07281h

rsc.li/materials-a

In this study we performed one-pot polycondensations of BFTB-4CHO with PyTA-4NH$_2$, BFTB-4NH$_2$, and BCTA-4NH$_2$ to prepare the bifluorenylidene-based covalent organic frameworks (COFs) BFTB–PyTA, BFTB–BFTB, and BFTB–BCTA, respectively. These three COFs possessed extremely high thermal stabilities, excellent crystallinities, and high specific surface areas. The BFTB–PyTA COF featured pores of a single size, whereas the BFTB–BFTB and BFTB–BCTA COFs had dual porosities. The COFs were exceptional adsorbers of the small dye molecule rhodamine B (RhB) in water; the maximum adsorption capacities reached as high as 2127 mg g^{-1}, outpacing those of all previously reported COFs, conjugated polymers, activated carbons, and other common nanoporous adsorbents. In addition, our COFs reached up to 99.2% of their maximum adsorption capabilities very rapidly (within 5 min). Furthermore, these COFs displayed good performance when used in electrodes for supercapacitors, with high stability after 2000 cycles. The superior adsorption efficiencies, ultrafast kinetics, and excellent reusability endow such COFs with tremendous potential for use as materials for removing RhB—and, presumably, other organic pollutants—from wastewater.

1. Introduction

Covalent organic frameworks (COFs)[1–3] comprise an emerging class of metal-free porous nanostructured polymers possessing precisely controllable structural features, inherent porosity, light weight, high crystallinity, high surface area, adjustable pore size, durability, and stability under a wide variety of thermal and chemical conditions; in addition, organic synthesis can be used to model, modify, and alter their chemical structures to achieve appropriate functions.[4–10] COFs show great promise for use in a diverse range of applications, including energy storage, gas uptake and separation, the detection and removal of toxic metal ions, sensing, catalysis, optoelectronics, photodynamic therapy, and solar cells.[11–22] The construction of COFs has typically relied on the formation of covalent bonds through irreversible condensation, leading to, for example, imine, triazine, benzoxazine, boronate, benzoxazole, hydrazone, borosilicate, and boroxine covalent linkages.[23–30] In particular, imine-linked COFs constructed from widely available organic aldehydes and amines have often exhibited high stability in most organic solvents and under harsh acidic or basic conditions, making them useful in a broad range of applications.[31,32] Nevertheless, the challenge is to develop new imine-linked COFs displaying exceptional porosity, crystallinity, and thermal stability.

Effective water remediation and purification are necessary to overcome problems related to shortage of safe water for human society.[33] Organic dyes are among the most common water pollutants, with wastewater from biological, industrial, and pharmaceutical activities frequently being polluted with them, potentially damaging the health of all living beings, the general public, and the ecosystem.[34–36] Most commercially used dyes are very toxic (even in small amounts), harmful to marine organisms, quite difficult to biodegrade, and carcinogenic along the

[a]Department of Materials and Optoelectronic Science, Center of Crystal Research, National Sun Yat-Sen University, Kaohsiung 80424, Taiwan. E-mail: kuosw@faculty.nsysu.edu.tw

[b]Chemistry Department, Faculty of Science, Assiut University, Assiut 71516, Egypt

[c]JST-ERATO Yamauchi Materials Space-Tectonics Project and International Research Center for Materials Nanoarchitectonics (WPI-MANA), National Institute for Materials Science (NIMS), 1-1 Namiki, Tsukuba, Ibaraki 305-0044, Japan

[d]Department of Chemistry, Faculty of Science, Tanta University, Tanta, Gharbeya 31527, Egypt

[e]School of Chemical Engineering, Australian Institute for Bioengineering and Nanotechnology (AIBN), The University of Queensland, Brisbane, Queensland 4072, Australia

[f]Ningbo Institute of Material Technology and Engineering, Chinese Academy of Science, Zhongguan West Road 1219, 315201 Ningbo, China

[g]JST-ERATO Yamauchi Materials Space-Tectonics Project, Kagami Memorial Research Institute for Materials Science and Technology, Waseda University, 2-8-26 Nishiwaseda, Shinjuku, Tokyo 169-0051, Japan

[h]Department of Medicinal and Applied Chemistry, Kaohsiung Medical University, Kaohsiung 807, Taiwan

† Electronic supplementary information (ESI) available. See DOI: 10.1039/d0ta07281h

ecological chain; therefore, their removal from wastewater is crucial.[34–36] Several strategies have, to date, been applied to eliminate organic dyes from wastewater using, for example, ion exchange and photocatalysis.[37] Adsorption strategies that are most likely to find widespread use will have to be eco-friendly and cost-effective. Many types of porous materials, such as zeolites, natural fibers, conjugated microporous polymers (CMPs), ordered mesoporous carbons (OMCs), and metal organic framework (MOFs), have been reported as dye adsorbents.[38–49] Zeolites and natural fibers typically suffer from poor removal performance, low adsorption efficiencies, and limited regeneration capabilities.[38–40] On the other hand, CMPs[41–43] and ordered mesoporous materials typically exhibit high removal efficiencies and rapid adsorption kinetics. However, CMPs are limited by the expensive catalysts used in their synthesis and their non-adjustable pore sizes, which would need to be controlled to maximize their dye removal efficiency. MOFs[44–46] suffer from low stabilities because they feature weakly coordinated metal–organic bonds. OMCs[47–49] are restricted by the requirement for treatment at high temperatures (up to 800 °C) during their preparation. Consequently, the quest remains to discover novel sorbents that operate with rapid adsorption kinetics and display exceptional adsorption performance for the removal and adsorption of pollutant dyes.

9,9′-Bifluorenylidene is a well-established non-fullerene-type electron acceptor featuring a dimerized fluorene structure. Once it accepts an electron, one of the fluorene rings becomes a 14π-electron system, and hence, aromaticity ensues.[50] In addition, because of the promising charge-transporting and electron-accepting properties of 9,9′-bifluorenylidene, its derivatives have been used as building blocks for the construction of hole-transport materials in perovskite solar cells and as the fullerene counterparts in bulk heterojunction solar cells.[51–53] To the best of our knowledge, bifluorenylidene-based COFs have not been reported previously. In this study, we prepared three bifluorenylidene-based COFs—BFTB–PyTA, BFTB–BFTB, and BFTB–BCTA—through one-pot reactions of 4,4′,4″,4‴-([9,9′-bifluorenylidene]-3,3′,6,6′-tetrayl)tetrabenzaldehyde (BFTB-4CHO) with 4,4′,4″,4‴-(pyrene-1,3,6,8-tetrayl) tetraaniline (PyTA-4NH$_2$), 4,4′,4″,4‴-([9,9′-bifluorenylidene]-3,3′,6,6′-tetrayl)tetraaniline (BFTB-4NH$_2$), and 4,4′,4″,4‴-([9,9′-bicarbazole]-3,3′,6,6′-tetrayl)tetraaniline (BCTA-4NH$_2$), respectively (Scheme 1). All of these COFs possessed high surface areas and extremely high thermal stabilities. Interestingly, they also exhibited exceptional adsorption capacities toward the small dye molecule rhodamine B (RhB) in water, achieving maximum adsorption capacities as high as 2127 mg g^{-1}—a value comparable with those of the best recently reported COFs and conjugated polymers. In addition, we investigated the suitability of these new COFs for energy storage.

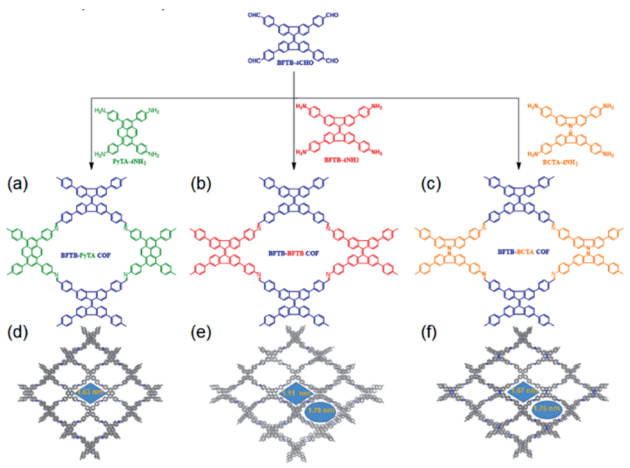

Scheme 1 (a–c) Synthesis and (d–f) top views of the AA-eclipsed models of the (a, d) BFTB–PyTA, (b, e) BFTB–BFTB, and (c, f) BFTB–BCTA COFs.

2. Results and discussion

2.1. Materials characterization

We synthesized PyTA-4NH$_2$ and BCTA-4NH$_2$ according to our recently reported procedures[54,55] and the new building blocks BFTB-4CHO and BFTB-4NH$_2$ readily through Suzuki–Miyaura reactions. The Pd-catalyzed condensations of 3,3′,6,6′-tetrabromo-9,9′-bifluorenylidene (BF-4Br) with 4-aminophenylboronic acid pinacol ester and 4-formylphenylboronic acid at 120 °C in 1,4-dioxane/water containing potassium carbonate led to BFTB-4NH$_2$ and BFTB-4CHO, respectively, in high yields. Fourier transform infrared (FTIR) and nuclear magnetic resonance (NMR) spectroscopy confirmed the chemical structures of our new building blocks. The FTIR spectrum of BFTB-4CHO exhibited absorption bands at 2812–2729, 1692, and 1598 cm^{-1} reflecting the stretching vibrations of its C(=O)–H, C=O, and C=C bonds, respectively (Fig. S1†); that of BFTB-4NH$_2$ displayed bands at 3453 and 3368 cm^{-1} for the stretching vibrations of N–H bonds and at 1598 and 1517 cm^{-1} representing the stretching vibrations of aromatic C=C bonds (Fig. S2†). The ^{1}H NMR spectrum of BFTB-4CHO featured a singlet at 10.10 ppm reflecting the resonance of the four aldehydic protons [C(=O)–H], as well as a set of signals in the range of 8.65–7.78 ppm for the aromatic protons (ArH); the spectrum of BFTB-4NH$_2$ featured a set of signals in the range of 8.32–6.71 ppm for the aromatic protons (ArH), in addition to a broad signal at 5.40 ppm for the resonance of the amino protons (N–H). The ^{13}C NMR spectrum of BFTB-4NH$_2$ displayed a signal at 148.93 ppm representing the nuclei of carbon atoms attached directly to amino groups (C–NH$_2$), in addition to a set of signals from 141.30–114.10 ppm representing the aromatic carbon nuclei.

Scheme 1 displays our syntheses of the three bifluorenylidene-based COFs BFTB–PyTA, BFTB–BFTB, and BFTB–BCTA COFs from the various building blocks. Solvothermal polycondensations of BFTB-4CHO with PyTA-4NH$_2$, BFTB-4NH$_2$, and BCTA-4NH$_2$ in a co-solvent of *n*-butanol/*o*-dichlorobenzene (1 : 1) containing acetic acid (6 M, 10 vol%) over 72 h at 110 °C in Schlenk tubes afforded the desired BFTB–PyTA, BFTB–BFTB, and BFTB–BCTA COFs, respectively, in high yields. The molecular structures of the as-prepared COFs were verified using FTIR and solid state ^{13}C NMR spectroscopy. The FTIR spectra of the BFTB–PyTA, BFTB–BFTB, and BFTB–BCTA COFs (Fig. S1–S3†) did not feature the distinctive vibration band

of the C=O bonds at 1692 cm^{-1} for BFTB-4CHO or the vibration bands of the N–H bonds in the ranges 3426–3344 cm^{-1} for PyTA-4NH_2, 3453–3368 cm^{-1} for BFTB-4NH_2, and 3437–3209 cm^{-1} for BCTA-4NH_2, implying successful polycondensations of BFTB-4CHO with the various tetraamines. New distinctive vibration bands for the imino (C=N) bonds appeared in the FTIR spectra of the BFTB–PyTA, BFTB–BFTB, and BFTB–BCTA COFs at 1623, 1622, and 1621 cm^{-1}, respectively. As expected, the solid state ^{13}C NMR spectra of the BFTB–PyTA, BFTB–BFTB, and BFTB–BCTA COFs featured distinctive signals at 175.74, 176.24, and 176.92 ppm, respectively, representing the resonances of their imino (C=N) carbon nuclei (Fig. 1a). In addition, signals for the aromatic carbon nuclei appeared in the ranges 144.92–112.73, 145.28–112.72, and 145.08–114.25 ppm in the ^{13}C NMR spectra of the BFTB–PyTA, BFTB–BFTB, and BFTB–BCTA COFs, respectively. The high degrees of polycondensation of these BFTB–PyTA, BFTB–BFTB, and BFTB–BCTA COFs were confirmed by their extremely high thermal stabilities. Fig. S4 and Table S1† reveal that our as-prepared COFs were thermally stable at high temperatures, as measured through thermogravimetric analysis (TGA) under a N_2 atmosphere. The BFTB–BCTA COF was the most thermally stable of our three COFs, with a decomposition temperature (T_{d10}) of approximately 449 °C and a char yield (after heating at 800 °C) of 71%; for the BFTB–PyTA COF, these values were 433 °C and 70%, respectively; for the BFTB–BFTB COF, they were 416 °C and 69%, respectively.

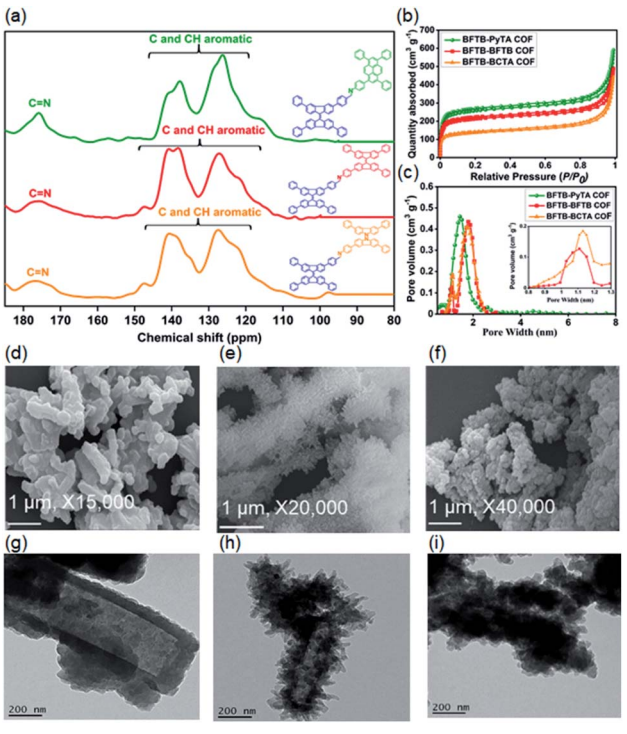

Fig. 1 (a) Solid state ^{13}C NMR spectra, (b) N_2 sorption isotherms at 77 K, and (c) pore size distributions of the BFTB–PyTA (olive), BFTB–BFTB (red), and BFTB–BCTA (orange) COFs. (d–f) FE-SEM and (g–i) TEM images of the (d, g) BFTB–PyTA, (e, h) BFTB–BFTB, and (f, i) BFTB–BCTA COFs.

We performed N_2 sorption isothermal analyses at 77 K to determine the porosity properties of the BFTB–PyTA, BFTB–BFTB, and BFTB–BCTA COFs. Fig. 1b reveals that all three of the as-prepared COFs provided type I isotherms with sharp N_2 uptake at lower pressure ($P/P_0 < 0.05$), indicative of microporous structures. We applied the Brunauer–Emmett–Teller (BET) model to evaluate the surface areas and pore volumes of the COFs. The BFTB–PyTA COF had the highest surface area of 1133 $m^2\ g^{-1}$ and a pore volume of 0.41 $cm^3\ g^{-1}$, with the BFTB–BFTB and BFTB–BCTA COFs having surface areas of 1040 and 834 $m^2\ g^{-1}$, respectively, and pore volumes of 0.69 and 0.67 $cm^3\ g^{-1}$, respectively (Table S2†). In addition, we used nonlocal density functional theory (NLDFT) to investigate the pore size distributions of our COFs, validating the single porosity of the BFTB–PyTA COF and the dual porosities of the BFTB–BFTB and BFTB–BCTA COFs. Fig. 1c and Table S2† reveal that the BFTB–PyTA COF exhibited a single micropore size of 1.63 nm, while the BFTB–BFTB (1.78 and 1.11 nm) and BFTB–BCTA (1.75 and 1.07 nm) COFs had two micropore sizes. We used field-emission scanning electron microscopy (FE-SEM) and transmission electron microscopy (TEM) to visualize the morphologies of the BFTB–PyTA, BFTB–BFTB, and BFTB–BCTA COFs. The FE-SEM images (Fig. 1d–f and S5†) revealed that the BFTB–PyTA COF assembled into smooth hollow microtubules. Most of these microtubules were consolidated into a set of bunches, but separate microtubules were also present, possibly a consequence of the sonication used for sample preparation. In contrast, the BFTB–BFTB COF assembled into hollow microtubules presenting a significant number of nanowires on their outer layers; these nanowires were distributed in random directions, creating a microsponge network. Similarly, most of the BFTB–BFTB COF microtubules were consolidated into a set of bunches, although separate microtubules were also present. The FE-SEM images of the BFTB–BCTA COF revealed continuously dispersed loose aggregates. TEM imaging (Fig. 1g–i and S6†) confirmed the hollow shapes and smooth surfaces of the BFTB–PyTA COF microtubules, the hollow shapes and sponge-like surfaces of the BFTB–BFTB COF microtubules, and the loosely aggregated morphology of the BFTB–BCTA COF. Statistical analyses of the TEM images of the BFTB–PyTA and BFTB–BFTB COFs provided average inner and outer diameters for the hollow tubular BFTB–PyTA COF of 400 ± 27 and 600 ± 30 nm, respectively; those of the hollow tubular BFTB–BFTB COF were 180 ± 21 and 240 ± 32 nm, respectively. These findings confirmed our recent observation that the degree of planarity of the building blocks strongly affects the final crystalline morphology of the resultant COFs. In this case, we obtained hollow tubular BFTB–PyTA and BFTB–BFTB COFs when reacting the most planar tetraamines PyTA-4NH_2 and BFTB-4NH_2.

We recorded powder X-ray diffraction (PXRD) patterns to gain insight into the crystalline nature of our synthesized COFs. The experimental PXRD data (black curves) of the BFTB–PyTA, BFTB–BFTB, and BFTB–BCTA COFs (Fig. 2a–c and S7–S9†) confirmed their excellent crystallinities, with the presence of intense peaks at values of 2θ of 4.53, 3.94, and 4.17°, respectively, matching the reflections from their [110] facets. The experimental PXRD pattern of the BFTB–PyTA COF featured

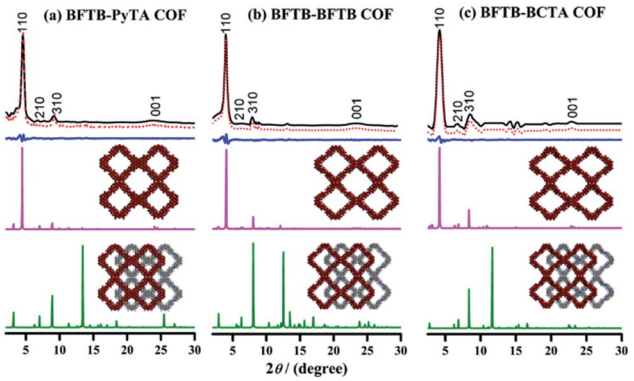

Fig. 2 (a–c) PXRD patterns of the (a) BFTB–PyTA, (b) BFTB–BFTB, and (c) BFTB–BCTA COFs: experimental patterns (black), simulated Pawley refined patterns (red), difference patterns (blue), and patterns simulated for the AA-eclipsed (purple) and AB-staggered (olive) stacking models.

additional peaks at values of 2θ of 6.71 and 9.10°, matching the reflections from its [210] and [310] facets; these reflections also appeared at 6.41 and 8.02° for the BFTB–BFTB COF and at 6.64 and 8.38° for the BFTB–BCTA COF. The reflections of the [001] facets appeared at values of 2θ of 23.90, 23.43, and 22.91° for the BFTB–PyTA, BFTB–BFTB, and BFTB–BCTA COFs, respectively. In addition, from these experimental PXRD patterns and the Bragg equation, we calculated the *d*-spacings (d_{110}) between the 110 planes and the π-stacking distances between the packed sheets of the synthesized COFs. As summarized in Table S2,† the BFTB–PyTA, BFTB–BFTB, and BFTB–BCTA COFs were distinguished by values of d_{110} of 1.94, 2.19, and 2.11 nm, respectively, and π-stacking distances of 3.71, 3.79, and 3.87 Å, respectively. To investigate the two-dimensional (2D) crystalline structures of the BFTB–PyTA, BFTB–BFTB, and BFTB–BCTA COFs, we used Material Studio software to simulate the plausible layered framework structures (AA-eclipsed and AB-staggered stacking) of these COFs and then to predict the simulated PXRD patterns of these stacking models. The simulated PXRD patterns (Fig. 2a–c, red curves) obtained from the Pawley refinement of the AA-eclipsed models fitted very well with the experimental peak positions (Fig. 2a–c and S7–S9,† black curves), as evidenced by their negligible differences (Fig. 2a–c, blue curves). In addition, comparisons of the resultant PXRD patterns for the AA-eclipsed (Fig. 2a–c and S7–S9,† purple curves) and AB-staggered (Fig. 2a–c, purple curves) stacking models with the experimental data revealed high consistency for the AA-eclipsed models and strong deviation from the AB-staggered models. These findings suggested that the 2D layered framework structures of the BFTB–PyTA, BFTB–BFTB, and BFTB–BCTA COFs were π-stacked eclipsed structures. Furthermore, we obtained the unit cell parameters of the BFTB–PyTA, BFTB–BFTB, and BFTB–BCTA COFs from refinements of their AA-eclipsed models: for the BFTB–PyTA COF, a = 24.918 Å, b = 31.042 Å, c = 3.528 Å, and $\alpha = \beta = \gamma = 90°$; for the BFTB–BFTB COF, a = 24.664 Å, b = 31.454 Å, c = 3.291 Å, and $\alpha = \beta = \gamma = 90°$; for the BFTB–BCTA COF, a = 31.909 Å, b = 28.274 Å, c = 4.073 Å, and $\alpha = \beta = \gamma = 90°$ (Fig. S10–S12 and Tables S3–S5†).

2.2. Dye removal

Integrating *N*-functionalized groups into the chemical structures of polymers can significantly improve their adsorption capacities toward organic pollutants in water. The high charge-density of nitrogen sites in these polymers can improve the interactions between the polymer and dye molecules, stabilized through a variety of noncovalent interactions.[56] Very recently, materials featuring high surface areas and wide-ranging pore volumes have been demonstrated to act as effective adsorbents for small sorbate molecules.[57] Notably, our BFTB–PyTA, BFTB–BFTB, and BFTB–BCTA COFs had excellent crystallinity, extremely high surface areas (up to 1133 $m^2\ g^{-1}$), large pore volumes (up to 0.69 $cm^3\ g^{-1}$), and contained imine (*N*-functionalized) groups. Therefore, we were encouraged to evaluate their suitability as organic adsorbents for the removal of dyes from water. Rhodamine B (RhB) is a popular organic cationic dye that is typically used as a standard guest to assess the adsorption efficiencies of adsorbents. We quantitatively estimated the adsorption efficiencies of the BFTB–PyTA, BFTB–BFTB, and BFTB–BCTA COFs by recording the UV-Vis spectra of aqueous solutions of RhB dye and monitoring the variation of the maximum adsorption peak at a λ_{max} of 554 nm at various time intervals (from 0 to 30 min) after the addition of the COFs (Fig. 3). Upon the addition of a very small amount of the BFTB–PyTA COF (4 mg) to an aqueous solution of RhB (10 mL, 25 mg L^{-1}), the intensity of the adsorption peak at 554 nm decreased by 40 and 85% within 1 and 3 min, respectively, while it disappeared fully within 5 min (Fig. 3a). The rapid uptake of RhB into this COF was confirmed by the turning of the dye

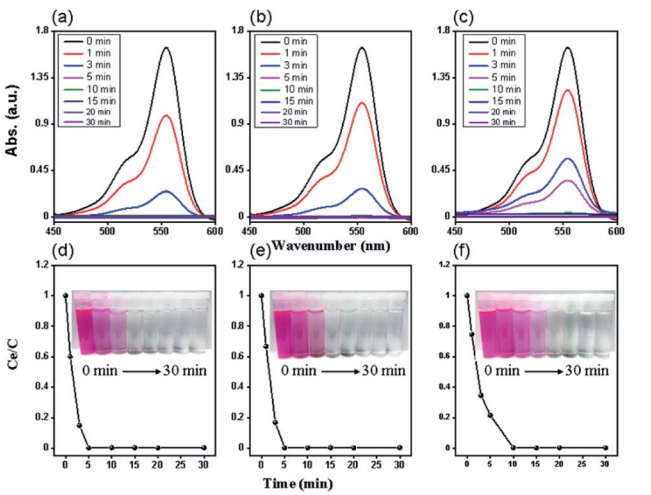

Fig. 3 (a–c) UV-Vis spectra of an aqueous RhB solution (initial concentration: 25 mg L^{-1}) at various time intervals after the addition of the (a) BFTB–PyTA, (b) BFTB–BFTB, and (c) BFTB–BCTA COFs. (d–f) Rates of adsorption of RhB from an aqueous solution (initial concentration: 25 mg L^{-1}) onto the (d) BFTB–PyTA, (e) BFTB–BFTB, and (f) BFTB–BCTA COFs, measured at various periods of time. Insets: corresponding photographs.

solution from deep violet-red to almost colorless within 5 min (inset to Fig. 3d). Thus, our new BFTB–PyTA COF displayed very high adsorption efficiency for the removal of this organic dye from water; the removal (within 5 min) percentage of RhB reached a maximum of 99.4% very rapidly (Fig. 3d). For the BFTB–BFTB COF, the adsorption peak at 554 nm also decreased by 33 and 83% within 1 and 3 min, respectively, while it disappeared totally within 5 min of the addition of the COF (4 mg) to an aqueous solution of RhB (10 mL, 25 mg L^{-1}) (Fig. 3b). Again, photographs of the dye solution revealed a color change from deep violet-red to almost colorless within 5 min of addition of the COF (inset to Fig. 3e). Indeed, the BFTB–BFTB COF also had a very high adsorption efficiency for the removal of RhB from water: the removal percentage reached 99.2% within 5 min (Fig. 3e). The BFTB–BCTA COF displayed relatively low efficiency for the dye removal from water. The adsorption peak at 554 nm decreased by 25, 65, and 79% within 1, 3, and 5 min, respectively, while it disappeared completely within 10 min after the addition of this COF (4 mg) to the dye solution (10 mL, 25 mg L^{-1}) (Fig. 3c). The inset to Fig. 3f reveals that the color of the aqueous dye solution changed from deep violet-red to almost colorless within 10 min of the addition of the COF; the removal percentage of RhB when using the BFTB–BCTA COF was 98.6% within 10 min (Fig. 3f).

These results suggest that four factors controlled the removal efficiency of RhB from water: surface area, morphology, and porosity of the COF, in addition to the π–π stacking interaction between the COFs and RhB. The dye removal efficiencies of the BFTB–PyTA and BFTB–BFTB COFs, with their relatively high surface areas and hollow structural morphologies, were higher than that of the BFTB–BCTA COF, which had the lowest surface area and a non-hollow structural morphology. For porosity, as previously reported, the pore size of the adsorbent material is one of the main factors deciding the adsorption efficiency toward organic dyes.[58,59] The adsorbent materials having pore sizes less than 1.5 nm showed low adsorption efficiency of dyes because almost all dye molecules have an average dimension higher than 1 nm, and thus, the pores of these adsorbents are blocked by the dye molecules. Otherwise, the adsorbent materials having pore sizes higher than 1.5 nm exhibited high adsorption efficiency for dyes. Such high pore sizes provided faster molecule transfer channels and sufficiently available storage spaces and surface areas, leading to the enhancement of both adsorption capacity and rate. Therefore, the BFTB–PyTA COF having a single pore size (1.63 nm) greater than the molecular size of RhB (1.59 × 1.18 × 0.56 nm) exhibited the highest dye removal efficiency. On the other hand, The BFTB–BFTB and BFTB–BCTA COFs having two pore sizes (1.78 and 1.11 nm) and (1.75 and 1.07 nm), respectively, showed less dye removal efficiency than the BFTB–PyTA COF due to the lower number of the large pores. Furthermore, as the π–π stacking interaction between the dye and adsorbent material increased, the adsorption capacity of the dye increased.[48] Based on the PXRD results, the π-stacking distances of the BFTB–PyTA, BFTB–BFTB, and BFTB–BCTA COFs were 3.71, 3.79, and 3.87 Å, respectively, indicating the stronger ability of the BFTB–PyTA COF to form π–π stacking interaction with aromatics than that of the BFTB–BFTB COF, which is higher than that of the BFTB–BCTA COF. This strongest π–π stacking interaction of the BFTB–PyTA COF is due to the presence of the highest aromaticity pyrene units in its structure, while the stronger π–π stacking interaction of the BFTB–BFTB COF than that of the BFTB–BCTA COF is due to the higher aromaticity of the bifluorenylidene units than that of the bicarbazole units. Therefore, the highest efficiency of the BFTB–PyTA COF for the dye removal from water could also be attributed to the presence of pyrene units in its structure which form strong π–π stacking interaction with the aromatic rings in the dye molecules. However, the higher dye removal efficiency of the BFTB–BFTB COF than that of the BFTB–BCTA COF is due to the stronger π–π stacking interaction between the aromatic rings in the dye molecule and the bifluorenylidene units in the BFTB–BFTB COF than that between the aromatic rings in the dye molecule and the bicarbazole units in the BFTB–BCTA COF. Moreover, the π–π stacking interactions between our COFs and dye molecules were confirmed by performing FTIR analyses of RhB and COFs before and after adsorption. As shown in Fig. S13–S15,† the FTIR spectrum of RhB was characterized by two bands at 1469 and 1590 cm^{-1} for the aromatic C=C bonds (Fig. S13b–S15b†). After the adsorption process, there is no notable change in the characteristic bands of our COFs, except for some shifting in the aromatic C=C bonds of the RhB and COFs, indicating the presence of π–π stacking interactions between the COFs and rhodamine B dye (Fig. S13d–S15d†).

We fitted the equilibrium adsorption data to the Langmuir isothermal model to study the adsorption behavior of RhB on the surfaces of our synthesized COFs. The Langmuir isothermal model provided good linear fits between the values of C_e/Q_e and the values of C_e (Fig. S16a†), with correlation coefficients (R_L^2) of 0.9903 for the BFTB–PyTA COF, 0.9891 for the BFTB–BFTB COF, and 0.9499 for the BFTB–BCTA COF (Table S6†). The adsorption capacity maxima (Q_m) of our COFs, predicted by their Langmuir isotherm models, were 2127 mg g^{-1} for the BFTB–PyTA COF, 1854 mg g^{-1} for the BFTB–BFTB COF, and 1605 mg g^{-1} for the BFTB–BCTA COF (Fig. S16b†). These values of Q_m are significantly higher than those of several recently reported COFs and conjugated polymers; they are also, to the best of our knowledge, the highest values for the adsorption of RhB on activated carbons and other common nanoporous adsorbents (Table S7†). Moreover, we conducted cyclic adsorption/regeneration experiments with the RhB solution to examine the recyclability of our BFTB–PyTA, BFTB–BFTB, and BFTB–BCTA COFs. The adsorption efficiencies of these COFs decreased insignificantly after five recovery cycles (Fig. S17†), indicating that our synthesized COFs have the potential to serve as efficient materials for removing organic pollutants from wastewater. Furthermore, the chemical stability of our COFs after five adsorption/regeneration cycles was investigated by FTIR and PXRD analyses. As shown in Fig. S18–S23,† the FTIR and PXRD peaks of BFTB–PyTA, BFTB–BFTB, and BFTB–BCTA COFs exhibited non-significant changes, indicating the high chemical stability of our synthesized COFs. Accordingly, we believe that our new COFs have great suitability for use as promising materials for removing organic pollutants from wastewater,

including anionic dyes as the adsorption process on our COFs does not depend on the electrostatic or acid–base interactions.

2.3. Supercapacitor applications

Very recently, COFs have also emerged as efficient electrodes for supercapacitors, due to the ability to add redox-active moieties into their frameworks by varying their building blocks. Furthermore, their high specific surface areas, uniform pore sizes, high crystallinity, and morphological and compositional tailorability make them attractive materials for energy storage. In this context, we fabricated electrodes by incorporating our BFTB–PyTA, BFTB–BFTB and BFTB–BCTA COFs and evaluated their performance using cyclic voltammetry (CV) and galvanostatic charge/discharge (GCD) methods. CV was performed at different scan rates in the range from 5 to 200 mV s^{-1} in a potential window from 0.0 to −1.0 V (*vs.* Ag/AgCl). The CV curves have symmetrical rectangle-like shapes, revealing that the capacitive response originated from electric double-layer capacitance (EDLC), similar to that for carbon materials (Fig. 4a–c).[60] Small humps appeared in the rectangle-like shapes in the cases of the BFTB–BFTB and BFTB–BCTA electrodes, indicating pseudocapacitance behavior, due to faradaic redox currents arising from the presence of the N heteroatoms.[5] The calculated gravimetric capacitances at different scan rates are shown in Fig. 4d and Table S8.†Interestingly, the BFTB–BCTA COF, having the lowest surface area of 834 m^2 g^{-1}, exhibited the highest specific capacitance of 89.9 F g^{-1} at 5 mV s^{-1} scan rate (Table S8†). This behavior is caused by the presence of the redox-active carbazole units[63] on the backbone, making the BFTB–BCTA COF effective in storing electrochemical energy and enhancing its specific capacitance. Although the BFTB–PyTA and BFTB–BFTB COFs had high surface areas of 1133 and 1040 m^2 g^{-1}, respectively, they provided lower specific capacitances of 68.0 and 84.5 F g^{-1} at 5 mV s^{-1} scan rate, respectively, because of the absence of the redox-active groups (Table S8†).

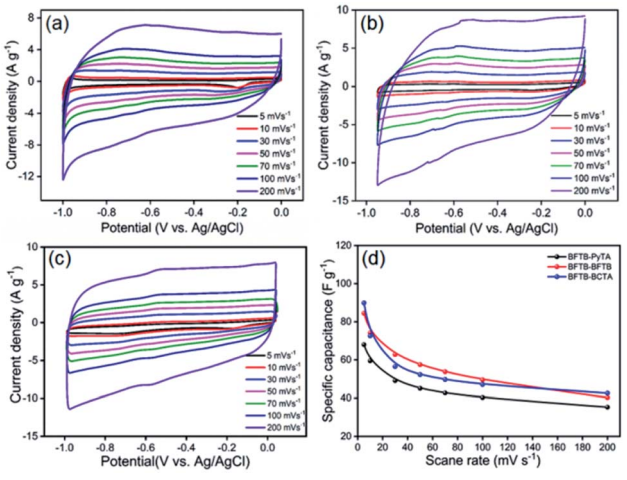

Fig. 4 (a–c) CV curves of the (b) BFTB–PyTA, (c) BFTB–BFTB, and (d) BFTB–BCTA electrodes measured at various scan rates (mV s^{-1}). (d) Gravimetric specific capacitance of the BFTB–PyTA, BFTB–BFTB and BFTB–BCTA electrodes at various scan rates.

The higher specific capacitance of the BFTB–BFTB COF than that of the BFTB–PyTA COF can be clarified by considering the surface-morphology of the COFs. As we reported, the hollow COF having a sponge-surface morphology showed higher specific capacitance than that having a smooth-surface morphology.[11,13] Therefore, the BFTB–BFTB COF featuring microsponge hollow tubules showed a higher capacitance than BFTB–PyTA which has smooth hollow microtubules.

We also investigated the long-term stability by cycling the electrodes at 10 A g^{-1} for 2000 cycles (Fig. S24†). The BFTB–PyTA, BFTB–BFTB, and BFTB–BCTA electrodes displayed high stability and robustness, with capacitive retentions of 97.27, 85.23, and 91.21%, respectively. BFTB–BFTB and BFTB–BCTA samples show almost similar behavior; however, BFTB–PyTA shows better retention. Due to the high retention of the BFTB–PyTA electrode, we performed the GCD measurement at current densities of 0.5, 1, 2, 3, 5, 7, 10, 15, and 20 A g^{-1} (Fig. 5a). The curves have triangular shapes, suggesting typical EDLC behavior.[5,61,62] At 1 A g^{-1}, the estimated specific capacitance of the BFTB–PyTA electrode is around 71 F g^{-1}. Notably, after increasing the current density to 20 A g^{-1}, the BFTB–PyTA electrode has a capacitance retention of around 50% (Fig. 5b). The electrochemical specific capacitance of the electrode prepared from our BFTB–PyTA COF is quite comparable to that of the previously reported COFs (Table S9†), suggesting that our COF materials might be useful as potential electrodes for energy storage applications.

The chemical stability and crystallinity of BFTB–PyTA, BFTB–BFTB, and BFTB–BCTA COFs in electrolyte were examined by immersing 60 mg of each COF in 1.0 M KOH solution for 3 days, which were then isolated using filtration, washed with H_2O, acetone, and THF three times, and finally dried at 100 °C. The FTIR and PXRD analyses of such isolated COFs showed approximately similar FTIR and PXRD peaks to those that appeared for the as-synthesized COFs (Fig. S18–S23†), revealing the high chemical stability and crystallinity of our COFs in the 1.0 M KOH electrolyte.

To estimate the capacitance contribution from the conductive additive carbon black used for preparing the electrode slurry, we conducted CV and GCD measurements on the bare carbon black electrode (Fig. S25†). It shows similar behavior of symmetrical rectangle-like CV curves, revealing that the capacitive response originated from electric double-layer capacitance

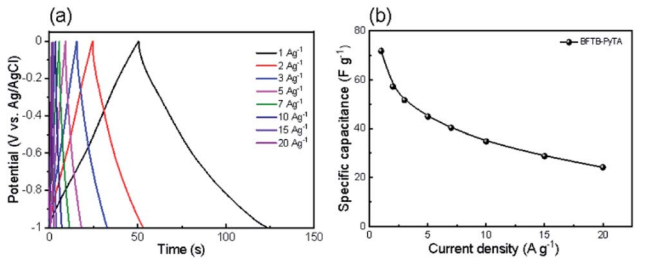

Fig. 5 (a) GCD curve of the BFTB–PyTA electrode measured at various current densities (A g^{-1}). (b) Calculated specific capacitances of the BFTB–PyTA electrode at various current densities.

(EDLC) of carbon materials (Fig. S25a†). Surprisingly the calculated specific capacitance from GCD measurements at 1 A g^{-1} was small (16.19 F g^{-1}), as shown in Fig. S25b.† The capacitance contribution from the carbon black electrode is small since it represents only 22% of the active BFTB–PyTA material.

3. Conclusions

We have prepared three new bifluorenylidene-based COFs that have extremely high thermal stabilities, high crystallinities, and large surface areas. Measurements of pore size distributions have revealed that the BFTB–PyTA COF has a single type of pore, while the BFTB–BFTB and BFTB–BCTA COFs have two types of heteropores with different sizes. We have tested these COFs for application in water treatment and energy storage. Our new bifluorenylidene-based COFs have great potential for use as adsorbents for removing trace pollutants from water. The BFTB–PyTA, BFTB–BFTB, and BFTB–BCTA COFs had extremely high adsorption capacities toward the organic RhB dye in water. In addition, their maximum adsorption capacities were successfully reached within a very short time frame (5 min). Our materials have also displayed good performance as electrodes for supercapacitors. Thus, this paper outlines a new strategy for the development of efficient bifluorenylidene-based COFs for the removal of RhB from wastewater and for energy storage. We believe that such materials appear to have great potential for use in various other domains in future.

Conflicts of interest

There are no conflicts to declare.

Acknowledgements

This study was supported financially by the Ministry of Science and Technology, Taiwan, under contracts MOST 106-2221-E-110-067-MY3, 108-2638-E-002-003-MY2, 108-2218-E-110-013-MY3, and 108-2221-E-110-014-MY3. This work was performed in part at the Queensland node of the Australian National Fabrication Facility (ANFF), a company established under the National Collaborative Research Infrastructure Strategy to provide nano and microfabrication facilities for Australia's researchers.

References

1 A. P. Cote, A. I. Benin, N. W. Ockwig, M. O'Keeffe, A. J. Matzger and O. M. Yaghi, *Science*, 2005, **310**, 1166–1170.
2 N. Huang, P. Wang and D. Jiang, *Nat. Rev. Mater.*, 2016, **1**, 16068–16086.
3 Y. Li, W. Chen, G. Xing, D. Jiang and L. Chen, *Chem. Soc. Rev.*, 2020, **49**, 2852–2868.
4 M. S. Lohse and T. Bein, *Adv. Funct. Mater.*, 2018, **28**, 1705553.
5 A. F. M. EL-Mahdy, M. G. Mohamed, T. H. Mansoure, H. H. Yu, T. Chen and S. W. Kuo, *Chem. Commun.*, 2019, **55**, 14890–14893.
6 K. E. Cordova and O. M. Yaghi, *Mater. Chem. Front.*, 2017, **1**, 1304–1309.
7 A. F. M. EL-Mahdy, C. H. Kuo, A. Alshehri, C. Young, Y. Yamauchi, J. Kim and S. W. Kuo, *J. Mater. Chem. A*, 2018, **6**, 19532–19541.
8 X. Chen, K. Geng, R. Liu, K. T. Tan, Y. Gong, Z. Li, S. Tao, Q. Jiang and D. Jiang, *Angew. Chem., Int. Ed.*, 2020, **59**, 5050–5091.
9 Y. Zhao, W. Dai, Y. Peng, Z. Niu, Q. Sun, C. Shan, H. Yang, G. Verma, L. Wojtas, D. Yuan and Z. Zhang, *Angew. Chem., Int. Ed.*, 2020, **59**, 4354–4389.
10 H. R. Abuzeid, A. F. M. EL-Mahdy and S. W. Kuo, *Microporous Mesoporous Mater.*, 2020, **300**, 110151.
11 A. F. M. El-Mahdy, Y.-H. Hung, T. H. Mansoure, H.-H. Yu, T. Chen and S. W. Kuo, *Chem.–Asian J.*, 2019, **14**, 1429–1435.
12 D. Dong, H. Zhang, B. zhou, Y. Sun, H. Zhang, M. Cao, J. Li, H. Zhou, H. Qian, Z. Lin and H. Chen, *Chem. Commun.*, 2019, **55**, 1458–1461.
13 A. F. M. El-Mahdy, C. Young, J. Kim, J. You, Y. Yamauchi and S. W. Kuo, *ACS Appl. Mater. Interfaces*, 2019, **11**, 9343–9354.
14 L. Zhang, S. Wang, Y. Zhou, C. Wang, X. Z. Zhang and H. Deng, *Angew. Chem., Int. Ed.*, 2019, **131**, 14351–14356.
15 A. F. M. EL-Mahdy, Y. H. Hung, T. H. Mansoure, H. H. Yu, Y. S. Hsu, K. C. Wu and S. W. Kuo, *J. Taiwan Inst. Chem. Eng.*, 2019, **103**, 199–208.
16 Y. Zeng, R. Zou and Y. Zhao, *Adv. Mater.*, 2016, **28**, 2855–2873.
17 L. A. Baldwin, J. W. Crowe, D. A. Pyles and P. L. McGrier, *J. Am. Chem. Soc.*, 2016, **138**, 15134–15137.
18 W. R. Cui, C. R. Zhang, W. Jiang, F. F. Li, R. P. Liang, J. Liu and J. D. Qiu, *Nat. Commun.*, 2020, **11**, 436.
19 P. Das and S. K. Mandal, *J. Mater. Chem. A.*, 2018, **6**, 16246–16256.
20 P. Pachfule, A. Acharjya, J. R. M. Roeser, T. Langenhahn, M. Schwarze, R. Schomacker, A. Thomas and J. Schmidt, *J. Am. Chem. Soc.*, 2018, **140**, 1423–1427.
21 X. Li, Q. Gao, J. Wang, Y. Chen, Z. H. Chen, H. S. Xu, W. Tang, K. Leng, G. H. Ning, J. Wu, Q. H. XU, S. Y. Queck, Y. Lu and K. P. Loh, *Nat. Commun.*, 2018, **9**, 2335.
22 C. Wu, Y. Liu, H. Liu, C. Duan, Q. Pan, J. Zhu, F. Hu, X. Ma, T. Jiu, Z. Li and Y. Zhao, *J. Am. Chem. Soc.*, 2018, **140**, 10016–10024.
23 X. Li, J. Qiao, S. W. Chee, H. S. Xu, X. Zhao, H. S. Choi, W. Yu, S. Y. Quek, U. Mirsaidov and K. P. Loh, *J. Am. Chem. Soc.*, 2020, **142**, 4932–4943.
24 M. G. Mohamed, A. F. M. EL-Mahdy, M. M. M. Ahmed and S. W. Kuo, *ChemPlusChem*, 2019, **84**, 1767–1774.
25 H. R. Abuzeid, A. F. M. EL-Mahdy, M. M. M. Ahmed and S. W. Kuo, *Polym. Chem.*, 2019, **10**, 6010–6020.
26 S. Park, Z. Liao, B. Ibarlucea, H. Qi, H. H. Lin, D. Becker, J. Melidonie, T. Zhang, H. Sahabudeen, L. Baraban, C. K. Baek, Z. Zheng, E. Zschech, A. Fery, T. Heine,

U. Kaiser, G. Cuniberti, R. Dong and X. Feng, *Angew. Chem., Int. Ed.*, 2020, **59**, 8218–8224.
27 P. F. Wei, M. Z. Qi, Z. P. Wang, S. Y. Ding, W. Yu, Q. Liu, L. K. Wang, H. Z. Wang, W. K. An and W. Wang, *J. Am. Chem. Soc.*, 2018, **140**, 4623–4631.
28 F. J. Uribe-Romo, C. J. Doonan, H. Furukawa, K. Oisaki and O. M. Yaghi, *J. Am. Chem. Soc.*, 2011, **133**, 11478–11481.
29 J. R. Hunt, C. J. Doonan, J. D. LeVangie, A. P. Côte and O. M. Yaghi, *J. Am. Chem. Soc.*, 2008, **130**, 11872–11873.
30 S. Ghosh, A. Nakada, M. Springer, T. Kawaguchi, K. Suzuki, H. Kaji, I. Baburin, A. Kuc, T. Heine, H. Suzuki, R. Abe and S. Seki, *J. Am. Chem. Soc.*, 2020, **142**, 9752–9762.
31 W. Huang, Q. He, Y. Hu and Y. Li, *Angew. Chem., Int. Ed.*, 2019, **131**, 8768–8772.
32 F. J. Uribe-Romo, J. R. Hunt, H. Furukawa, C. Klock, M. O'Keeffe and O. M. Yaghi, *J. Am. Chem. Soc.*, 2009, **131**, 4570–4571.
33 B. Chen, Q. Ma, C. Tan, T. T. Lim, L. Huang and H. Zhang, *Small*, 2015, **11**, 3319–3336.
34 A. A. Adeyemo, I. O. Adeoye and O. S. Bello, *Environ. Toxicol. Chem.*, 2012, **94**, 1846–1863.
35 V. K. Gupta, R. Kumar, A. Nayak, T. A. Saleh and M. A. Barakat, *Adv. Colloid Interface Sci.*, 2013, **193**, 24–34.
36 V. K. Sharma and M. Feng, *J. Hazard. Mater.*, 2019, **372**, 3–16.
37 S. M. Wang, D. L. Li, C. Sun, S. G. Yang, Y. Guan and H. He, *Appl. Catal., B*, 2014, **144**, 885–892.
38 M. Rafatullah, O. Sulaiman, R. Hashim and A. Ahmad, *J. Hazard. Mater.*, 2010, **177**, 70–80.
39 M. F. Cheira, M. N. Rashed, A. E. Mohamed, I. H. Zidan and M. A. Awadallah, *Sep. Sci. Technol.*, 2019, 1.
40 K. Roy, A. Mukherjee, N. R. Maddela, S. Chakraborty, B. Shen, M. Li, D. Du, Y. Peng, F. Lu and L. C. Cruzatty, *J. Environ. Chem. Eng.*, 2020, **8**, 103572.
41 S. Das, P. Heasman, T. Ben and S. Qiu, *Chem. Rev.*, 2017, **117**, 1515–1563.
42 Z. Wang, S. Guo, B. Zhang, J. Fang and L. Zhu, *J. Hazard. Mater.*, 2020, **384**, 121187.
43 P. C. Chang, L. Zhu, J. M. Tan, B. Liu, X. L. Tan and H.-B. Xu, *Macromolecules*, 2015, **48**, 8509–8514.
44 P. Z. Li, X. J. Wang and S. Y. Tan, *Angew. Chem., Int. Ed.*, 2015, **54**, 12748–12752.
45 A. Kirchon, P. Zhang, J. Li, E. A. Joseph, W. Chen and H. C. Zhou, *ACS Appl. Mater. Interfaces*, 2020, **12**, 9292–9299.
46 P.-Q. Liao, X.-W. Chen and S.-Y. Liu, *Chem. Sci.*, 2016, **7**, 6528–6533.
47 J. Wang, Y. Wang, H. Hu, Q. Yang and J. Cai, *Nanoscale*, 2020, **12**, 4238–4268.
48 A. F. M. EL-Mahdy, T. E. Liu and S. W. Kuo, *J. Hazard. Mater.*, 2020, **391**, 122163.
49 J. Gong, H. Lin, M. Antonietti and J. Yuan, *J. Mater. Chem. A*, 2016, **4**, 7313–7321.
50 H. U. Kim, J. H. Kim, J. B. Park, J. Kwak, W. S. Shin, S. C. Yoon and D. H. Hwang, *Sol. Energy Mater. Sol. Cells*, 2013, **116**, 275–282.
51 K. Rakstys, M. Saliba, P. Gao, P. Gratia, E. Kamarauskas, S. Paek, V. Jankauskas and M. K. Nazeeruddin, *Angew. Chem., Int. Ed.*, 2016, **55**, 7590–7594.
52 F. G. Brunetti, X. Gong, M. Tong, A. J. Heeger and F. Wudl, *Angew. Chem., Int. Ed.*, 2010, **49**, 532–536.
53 N. G. Park and K. Zhu, *Nat. Rev. Mater.*, 2020, **5**, 333–350.
54 A. F. M. EL-Mahdy, A. M. Elewa, S. W. Huang, H. H. Chou and S. W. Kuo, *Adv. Opt. Mater.*, 2020, **8**, 2000641.
55 A. F. M. EL-Mahdy, M. Y. Lai and S. W. Kuo, *J. Mater. Chem. C*, 2020, **8**, 9520–9528.
56 Y. Yuan, H. Huang, L. Chen and Y. Chen, *Macromolecules*, 2017, **50**, 4993–5003.
57 T. Ben, H. Ren, S. Ma, D. Cao, J. Lan, X. Jing, W. Wang, J. Xu, F. Deng, J. M. Simmons, S. Qiu and G. Zhu, *Angew. Chem., Int. Ed.*, 2009, **48**, 9457–9460.
58 L. Li, F. Sun, J. Gao, L. Wang, X. Pi and G. Zhao, *RSC Adv.*, 2018, **8**, 14488–14499.
59 S. C. Smith and D. F. Rodrigues, *Carbon*, 2015, **91**, 122–143.
60 R. R. Salunkhe, J. Wang, A. Alowasheeir, J. Lin, V. Malgras, Y. Bando, M. B. Zakaria, A. A. Alshehri, J. Kim, Y. Yamauchi and K. C. W. Wu, *ChemistrySelect*, 2018, **3**, 4522–4526.
61 A. Azhar, Y. Yamauchi, A. E. Allah, Z. A. Alothman, A. Y. Badjah, M. Naushad, M. Habila, S. Wabaidur, J. Wang and M. B. Zakaria, *Nanomaterials*, 2019, **9**, 776.
62 A. Azhar, M. B. Zakaria, J. Lin, T. Chikyow, D. J. Martin, Y. G. Alghamdi, A. A. Alshehri, Y. Bando, M. S. A. Hossain, K. C. W. Wu, N. A. Kumar and Y. Yamauchi, *ChemistrySelect*, 2018, **3**, 8505–8510.
63 S.-H. Hsiao and S.-W. Lin, *Polym. Chem.*, 2016, **7**, 198–211.